Remote Sensing of Environment 201 (2017) 331–341

Contents lists available at ScienceDirect

Remote Sensing of Environment

journal homepage: www.elsevier.com/locate/rse

Remote sensing of chlorophyll-*a* in coastal waters based on the light absorption coefficient of phytoplankton

Guangming Zheng[a,b,*], Paul M. DiGiacomo[a]

[a] NOAA/NESDIS Center for Satellite Application and Research, 5830 University Research Court, College Park, MD 20740, USA
[b] Global Science & Technology, Inc., 7855 Walker Drive, Suite 200, Greenbelt, MD 20770, USA

ARTICLE INFO

Keywords:
Chlorophyll
Turbid coastal water
Light absorption coefficient
Partitioning
Stacked-constraints approach

ABSTRACT

Remote sensing of chlorophyll-*a* concentration, [Chl-*a*], has been difficult in coastal waters like the Chesapeake Bay owing largely to terrestrial substances (such as minerals and humus) that are optically significant but do not covary with phytoplankton. Here we revisit the semi-analytical pathway of deriving [Chl-*a*] based on the light absorption coefficient of phytoplankton by introducing the generalized stacked-constraints model (GSCM) to partition satellite-derived total light absorption coefficient of water (with pure-water contribution subtracted), $a_{nw}(\lambda)$, into phytoplankton, $a_{ph}(\lambda)$, and non-phytoplankton components, where $a_{nw}(\lambda)$ is derived from satellite remote-sensing reflectance, $R_{rs}(\lambda)$, using the Quasi-Analytical Algorithm. The GSCM-derived $a_{ph}(\lambda)$ was compared with field matchups of [Chl-*a*]. We show that semi-analytical approaches can provide superior [Chl-*a*] product compared with reflectance-band-ratio algorithms when the accuracy of satellite-derived $a_{ph}(\lambda)$ is sufficiently improved, in this case with the GSCM. However, the improvement is at the cost of significantly reduced data availability because the GSCM may provide no feasible solutions when input $a_{nw}(\lambda)$ data are subject to large errors. This in turn highlights the needs for improved atmospheric correction and upstream models capable of preserving actual spectral shapes of $R_{rs}(\lambda)$ and $a_{nw}(\lambda)$, respectively.

1. Introduction

Phytoplankton constitute the base of aquatic food web and are a primary driver of biogeochemical processes in the ocean. As such, phytoplankton biomass is a key parameter for oceanographic and biogeochemical research and applied studies. In coastal waters, phytoplankton biomass serves as an important water quality parameter since the abundance of algae can potentially indicate the degree of eutrophication in a specific water body. In practice, phytoplankton biomass is typically quantified with a proxy, e.g., by measuring the concentration of chlorophyll-*a*, [Chl-*a*], which is a ubiquitous photosynthetic pigment present in all algal species. Measurements of [Chl-*a*] can be made in situ (e.g., chlorophyll fluorometers), remotely (e.g., optical radiometers), as well as in the lab through discrete water sample analyses (e.g., Dickey et al., 2006). Albeit generally less accurate than other data methods, remote sensing (especially via satellite platforms) is typically the most efficient and cost-effective measure for users because it enables synoptic sampling at basin, regional, and local scales with high revisit frequency (potentially up to several times per day).

Currently, there are no universally accepted algorithms for accurately deriving [Chl-*a*] in coastal waters from the remote-sensing reflectance, $R_{rs}(\lambda)$, where λ is light wavelength in vacuum. Unlike the open oceans where phytoplankton drive the variation of inherent optical properties of water, coastal waters are subject to influences from terrestrially originated materials such as humus and iron-rich minerals which contribute significantly to the light absorption and scattering in water, but do not covary with phytoplankton. As a result, the standard blue-to-green reflectance-band-ratio algorithms that are acceptable to address the open oceans (e.g., O'Reilly et al., 1998) are inadequate for coastal waters, as has been reported widely (e.g., Magnuson et al., 2004; Tzortziou et al., 2007; Werdell et al., 2009). There have been more advanced algorithms such as the neural network approach developed for coastal waters (e.g., Alimonte and Zibordi, 2003; González Vilas et al., 2011; Tanaka et al., 2004), which essentially apply a greater number of fixed coefficients to the input reflectance data. However, the optical properties of coastal waters are highly dynamic and such algorithms have not proven suitable for diverse water types. In addition to the blue and green bands, the red and near-infrared (NIR) bands have also been used as a basis to derive [Chl-*a*] from remote-sensing data. A benefit of using longer wavelengths is the reduced influence from light absorption of non-algal suspended particles and colored dissolved

* Corresponding author.
E-mail address: guangming.zheng@noaa.gov (G. Zheng).

http://dx.doi.org/10.1016/j.rse.2017.09.008
Received 11 January 2017; Received in revised form 27 August 2017; Accepted 12 September 2017
Available online 26 September 2017

organic matter (CDOM) on the derived [Chl-*a*] product (e.g., Dall'Olmo et al., 2005; Gitelson et al., 2007; Gons et al., 2002; Moses et al., 2009) because their absorption coefficients drop exponentially with wavelength. This type of algorithms appear to perform fairly well for intense algal blooms ([Chl-*a*] > tens of mg m^{-3}) but suffer from low signal-to-noise ratio for lower-biomass scenarios.

Phytoplankton are efficient light absorbers at the blue and red bands owing to presence of intracellular pigments, but not effective contributors to total backscattering coefficient compared with minerals which have higher density and lower water content, or colloidal particles which are more abundant and have larger backscattering-to-scattering ratio (Aas, 1996; Stramski et al., 2004; Stramski and Kiefer, 1991). As a result, the remote sensing of phytoplankton generally relies on the detection of its light absorption signal. However, non-phytoplankton materials often compete strongly with phytoplankton in contribution to the total light absorption coefficient. Therefore, separation of phytoplankton and non-phytoplankton light absorption signals, as is addressed by more physics-based "semi-analytical" algorithms (e.g., Lee et al., 2002; Maritorena et al., 2002; Smyth et al., 2006), are desirable to obtain improved [Chl-*a*] products. One might expect that empirical algorithms that associate [Chl-*a*] directly with some combinations of $R_{rs}(\lambda)$ and do not discriminate between phytoplankton and nonalgal pigmenting agents are more likely than semi-analytical models to mismatch [Chl-*a*] with the light absorption and backscattering signals contributed by materials that may have nothing to do with phytoplankton. In this regard, the results of a round-robin test conducted by Brewin et al. (2015) are somewhat counter-intuitive. Using field data obtained in both open ocean and coastal waters, they found that a group of 5 empirical algorithms consistently outperformed another group of 11 semi-analytical ones with respect to the accuracy of derived [Chl-*a*].

Does it imply that semi-analytical approaches are merely conceptually superior but practically less effective than empirical ones with respect to the remote sensing of [Chl-*a*] in oceanic and coastal waters? We note that the semi-analytical models evaluated by Brewin et al. (2015) impose highly restrictive assumptions on the spectral shapes of the light absorption coefficient of phytoplankton, $a_{ph}(\lambda)$, and non-phytoplankton materials. These assumptions are inadequate for resolving bio-geo-optical variability in coastal waters and might have adversely affected the accuracy of these models. Recently, Zheng et al. (2015) developed a Generalized Stacked-Constraints Model (GSCM) which relaxed these restrictive assumptions. The GSCM takes the input of the total non-water absorption coefficient, $a_{nw}(\lambda)$, either field-measured or remotely sensed, and partitions it into $a_{ph}(\lambda)$ and nonalgal components. Although the model was shown to be capable of partitioning the field-measured $a_{nw}(\lambda)$ with reasonable accuracy, it is unclear whether the GSCM can enable semi-analytical [Chl-*a*] models to outperform empirical ones simply by improving the accuracy of satellite-derived $a_{ph}(\lambda)$. This is because in the remote-sensing context the GSCM must be combined with an "upstream" model that derives the required $a_{nw}(\lambda)$ from $R_{rs}(\lambda)$, and additionally satellite-measured $R_{rs}(\lambda)$ is subject to many sources of uncertainties such as calibration and atmospheric-correction issues. Can GSCM help advance the remote sensing of [Chl-*a*] beyond empirical reflectance-band-ratio algorithms? This study explores answers to this question.

2. Data and methods

Field measurements of [Chl-*a*] were matched up with satellite-derived $R_{rs}(\lambda)$ data based on sampling time and location. A matchup was considered valid when satellite and field observations were made within 3 h and 1 km. The field-measured [Chl-*a*] data were obtained from the Chesapeake Bay Program (CBP, http://www.chesapeakebay.net/) which is a long-term field sampling network established since 1984. For the present study only data collected since September 1997 were used with a cutoff on December 2016, covering the current era of sustained satellite ocean color observations. The satellite data used for match-up were collected by four sensors including the Sea-Viewing Wide Field-of-View Sensor (SeaWiFS), the Moderate Resolution Imaging Spectroradiometer (MODIS) onboard Aqua, the MEdium Resolution Imaging Spectrometer (MERIS), and the Visible Infrared Imaging Radiometer Suite (VIIRS). Matchups from all four sensors during the period of 1997–2015 were used to develop a new [Chl-*a*] model based on the semi-analytical approach, hereafter referred to as the development dataset. Matchups from VIIRS in the year 2016 were used as independent data to evaluate performance of the new model, hereafter referred to as the validation dataset. The majority of matchup data were included in the development dataset to obtain more robust regression coefficients for the new model. Below we describe the field and satellite data in detail.

2.1. Field data of chlorophyll-a concentration

The Chesapeake Bay program provides regular field observations of 19 water quality parameters at 49 stations in the Chesapeake Bay mainstem as well as hundreds of other stations in its tributaries. Stations were generally sampled monthly except during summer when sampling took place twice a month. Sometimes additional sampling was conducted after significant weather events. Figure 1 shows the locations of a total of 64 sampling stations that were used for satellite match-ups. These stations were selected to maximize the availability of field data while still maintaining reasonable distance from land to minimize the adjacency effect in satellite imagery caused by light scattered from brighter pixels (such as land) to the field of view of neighboring water pixels. The selected stations include those named after CB2, CB3, CB4, CB5, CB6, CB7, CB8, EE, ET, LE, TF, WE, and WT. At each station, chlorophyll samples were collected at the surface and bottom, and at two additional depths depending on the existence and location of a pycnocline. For this study we used only surface chlorophyll data

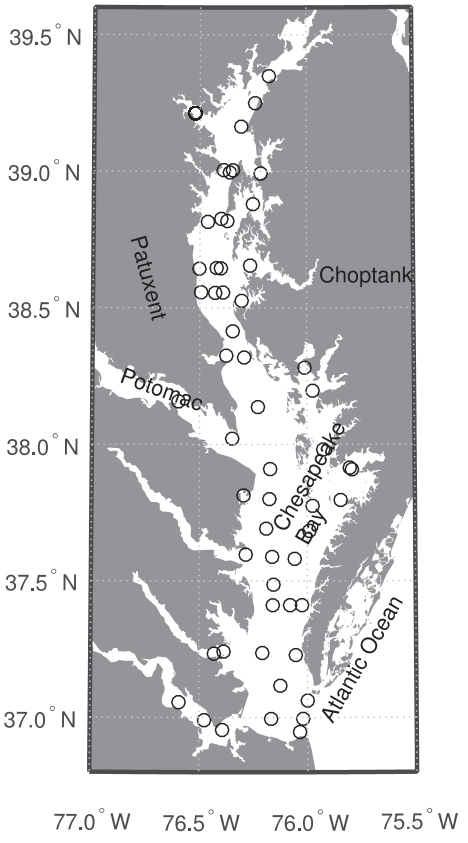

Fig. 1. Sampling stations of the Chesapeake Bay Program selected for this study.

(0–1 m), which were measured by Maryland Department of Health and Mental Hygiene (DHMH), Chesapeake Biological Laboratory, Old Dominion University Applied Marine Research Laboratory, and Virginia Division of Consolidated Laboratory Services (DCLS).

The protocol used to determine [Chl-*a*] is consistent across different stations. It is a monochromatic method conforming to the American Society for Testing and Materials (ASTM) and includes a correction for pheophytin. Here we describe only the general procedures of this protocol. More details are provided in the report by Olson (2012) and ASTM (2012). Specifically, each water sample was filtered through a GF/F filter and then subjected to acetone extraction. The acetone extract was then centrifuged and the clear supernatant was measured using a spectrophotometer to obtain the spectral optical density (OD) associated with light absorption. Subsequently, the acetone solution is acidified with HCl and re-measured for the OD. The final formula is:

$$[Chl\text{-}a] = 26.7\,[(OD_{664B} - OD_{750B}) - (OD_{665A} - OD_{750A})]\,l\,V_{extract} / V_{sample} \ \text{mg m}^{-3},$$

where

OD_{664B} and OD_{750B}, OD of acetone extract before acidification at 664 and 750 nm, respectively;

OD_{665A} and OD_{750A}, OD of acetone extract after acidification at 665 and 750 nm, respectively;

l, light pathlength through acetone extract in cm;
$V_{extract}$, total volume of acetone extract in L;
V_{sample}, total volume of water sample filtered in m^3.

Figure 2 gives an overview of all [Chl-*a*] measured at the selected stations during the time period of the matchup analysis. It shows that the most frequent [Chl-*a*] values encountered in the Chesapeake Bay surface waters are within 6–8 mg m^{-3}. More than 95% of the samples have [Chl-*a*] lower than 30 mg m^{-3}.

2.2. Satellite data of remote-sensing reflectance

Satellite-derived normalized water-leaving radiance, $nL_w(\lambda)$, data are "Level-2" products generated after the application of instrument calibration, vicarious calibration, and atmospheric correction. As calibrations update, raw data recorded as digital counts ("Level-0") need to be reprocessed and the derived Level-2 products are subject to change. Satellite data used in this study are as follows: NASA versions "R2014.0" for SeaWiFS, "R2012.1" for MERIS, and "R2014.0.1" for MODIS-Aqua data, and NOAA version "SCI_OC03_V1.10" (in development dataset, 1997–2015) and "SCI_OC04.0_V1.20" (in validation dataset, 2016) for VIIRS data. With respect to schemes of atmospheric correction, data

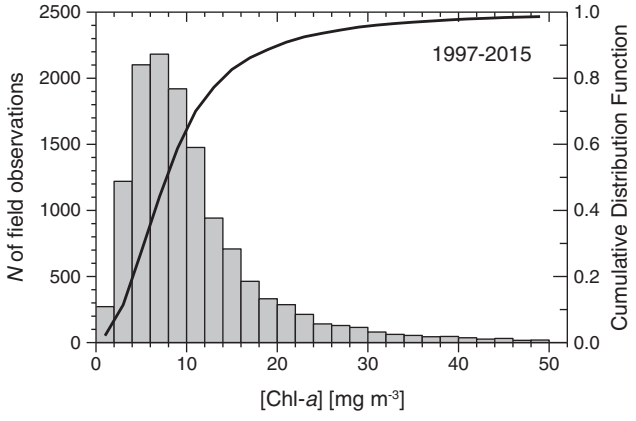

Fig. 2. Histogram of surface chlorophyll concentration measured at the Chesapeake Bay Program stations during 1997–2015. Bars refer to the left axis. The curve refers to the right axis.

obtained from NASA were generated using the NIR bands as a basis for making the "black-pixel" assumption, hereafter referred to as NIR-corrected data (see references cited in http://oceancolor.gsfc.nasa.gov/cms/reprocessing/AtmoCor.html). Two streams of VIIRS ocean color data produced by NOAA were used in this study. One stream adopts the "BMW" atmospheric correction algorithm (Jiang and Wang, 2014) which is essentially a variant of the NIR-based scheme and combines the three algorithms developed by Bailey et al. (2010), Ruddick et al. (2000), and Wang et al. (2012). Another stream of VIIRS data were processed with an atmospheric correction scheme that replaces the NIR bands with shortwave infrared (SWIR) bands, hereafter referred to as SWIR-corrected data (described by Wang et al., 2007). Using the same algorithm, SWIR-corrected data were also produced for MODIS-Aqua over the period of 2002–2013 using the "Level-1b" data (version 5) obtained from the NASA MODIS Adaptive Processing System (MODAPS) Services website (https://ladsweb.nascom.nasa.gov/). The SWIR-corrected data have meaningful values in the NIR, and are essential to evaluating the performance of algorithms that utilize NIR bands.

The final spectral reflectance $R_{rs}(\lambda)$ is calculated as the $nL_w(\lambda)$ divided by the extraterrestrial solar irradiance, $F_0(\lambda)$.

2.3. Satellite data processing steps

The $R_{rs}(\lambda)$ data for coastal waters like the Chesapeake Bay are often significantly affected by terrestrial originated materials such as minerals and humus. To use the GSCM to distinguish the contribution of phytoplankton to the overall optical signal, input of total absorption coefficient $a_{nw}(\lambda)$ is required. In this study, the Quasi-Analytical Algorithm (QAA) (Lee et al., 2002) version 6 (http://www.ioccg.org/groups/software.html) was chosen as the upstream model that derives $a_{nw}(\lambda)$ from $R_{rs}(\lambda)$. The $a_{ph}(\lambda)$ obtained by partitioning the QAA-derived $a_{nw}(\lambda)$ with the GSCM was compared with field-measured [Chl-*a*]. Figure 3 shows the three main steps of satellite data processing.

The objective of Step 1 is to remove questionable $R_{rs}(\lambda)$ spectra and minimize their impact on subsequent comparisons of algorithm performance. Specifically, the satellite-derived $R_{rs}(\lambda)$ used in this study often drops quickly towards the short wavelengths (~410 and 440 nm), sometimes even below zero, suggesting a possible over-estimation of atmospheric contribution to the total top-of-atmosphere radiance during the atmospheric correction process. For this purpose we used the

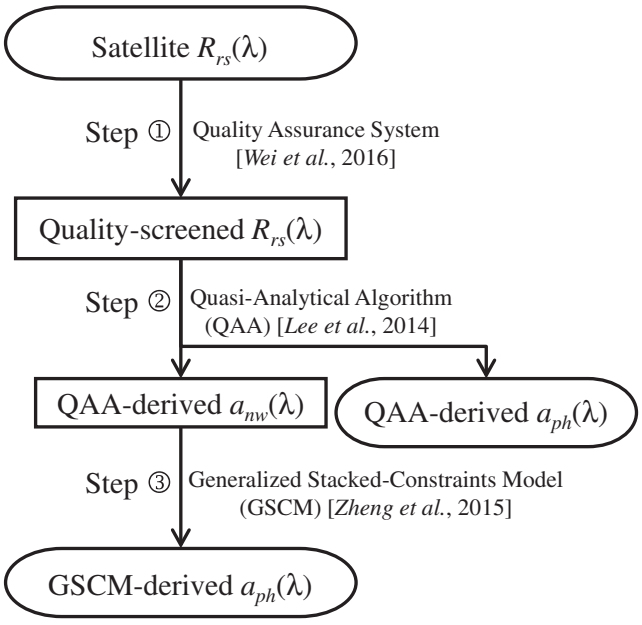

Fig. 3. Flowchart of satellite data processing. Rounded text boxes highlight input and output variables. Normal text boxes highlight intermediate variables.

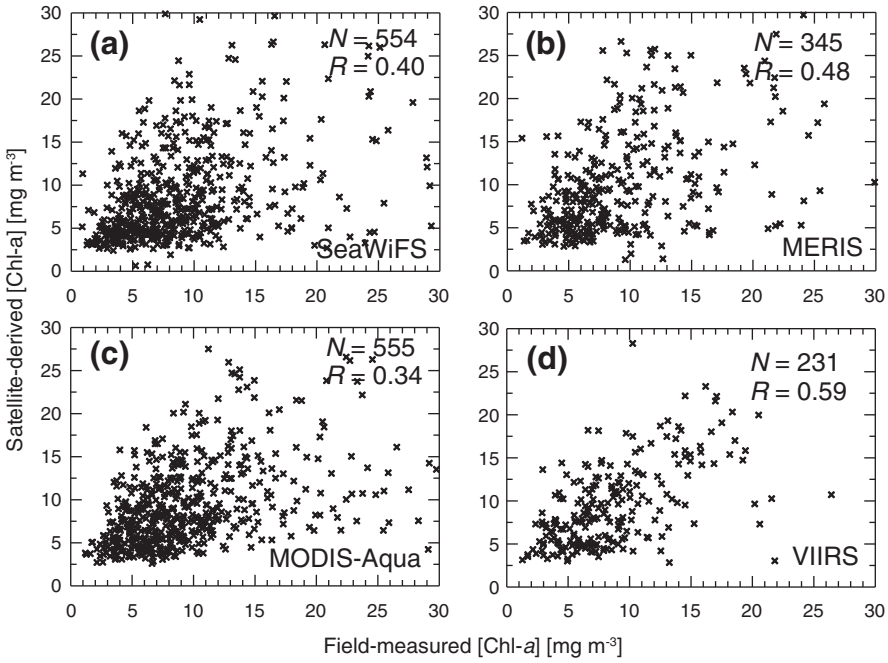

Fig. 4. The [Chl-*a*] derived from (a) SeaWiFS, (b) MERIS, (c) MODIS-Aqua, and (d) VIIRS measurements using the blue-to-green reflectance band ratio of $R_{rs}(490)/R_{rs}(550)$ (Eq. 1), plotted versus field-measured values in the Chesapeake Bay for the development dataset. *N*, number of matchups. *R*, correlation coefficient.

"quality assurance system" developed by Wei et al. (2016), which defines 23 optical water types based on a cluster analysis of 958 quality-verified $R_{rs}(\lambda)$ spectra. For a given $R_{rs}(\lambda)$ with unknown quality, in this case a satellite-derived spectrum, this approach first identifies the closest water type based on the spectral shape of normalized spectra, and then assign a score for each individual wavelength based on the degree of departure of the given spectrum from the mean spectrum of that water type. If the departure exceeds trusted ranges, a score of 0 is assigned at that wavelength, otherwise a score of 1 is assigned. In our analysis, we included only wavelengths of ~410, 440, 490, 550, and 670 nm which are the required input bands of the GSCM, and accepted only spectra that scored 1 across all 5 wavelengths.

Step 2 is to obtain $a_{nw}(\lambda)$ from $R_{rs}(\lambda)$. The QAA was chosen here because it is conceptually consistent with the GSCM in terms of the sequence of deriving total and component absorption coefficients, and its accuracy is relatively well understood for moderately turbid shelf waters (e.g., Mitchell et al., 2014; Zheng et al., 2014). In the implementation of QAA we used the 670 nm as the only reference band (see calculation formulas described in version 6, http://www.ioccg.org/groups/Software_OCA/QAA_v6_2014209.pdf). We found this approach more suitable for the Chesapeake Bay waters than using 550 nm as the reference band (results not shown) and it ensures smooth model outputs when $R_{rs}(670)$ changes across 0.0015 sr^{-1}, where the original QAA version 6 requires a band switch and introduces unwanted, abrupt changes in outputs. With respect to the Raman scattering effect on $R_{rs}(\lambda)$ and the temperature/salinity effect on pure water optical properties, no corrections were applied because they are considered insignificant for the spectral range and water properties addressed in this study.

In Step 3 we partitioned the QAA-derived $a_{nw}(\lambda)$ using the GSCM to obtain the contribution attributable to phytoplankton, $a_{ph}(\lambda)$. This model uses a set of 7 normalized spectra of nonalgal particulate absorption coefficient, $a_d(\lambda)$, and 5 CDOM absorption coefficient, $a_g(\lambda)$, determined from cluster analysis of field-measured data collected in the Chesapeake Bay, which is a significant improvement in terms of accounting for the variability of their spectral shapes compared with the typically adopted exponential function of λ. During implementation, the GSCM first mix and match various combinations of $a_d(\lambda)$ and $a_g(\lambda)$ spectra to derive a large number of speculative solutions, and then constrain the solution space with a set of inequality constraints which allow for adequate range of variability. The inequality constraints in the GSCM essentially define the permitted range of variation in the spectral shape of $a_{ph}(\lambda)$ ($a_d(\lambda)$ as well), which were determined based on the 1st and 99th percentiles of a set of $a_{ph}(\lambda)$ band-ratios as observed in field data (see Zheng et al., 2015 for details). Different from other inverse models, the GSCM does not necessarily provide a final output, which happens when no feasible solutions can be identified despite of the flexibility allowed by the inequality constraints. However, when feasible solutions of the $a_{ph}(\lambda)$ are identified, it is guaranteed that they all exhibit reasonable spectral shapes, at least at the 5 bands involved by the in equality constraints.

3. Results and discussions

3.1. Evaluation of empirical [Chl-a] algorithms using the development dataset

To compare with the results derived from the GSCM, we first evaluate the accuracy of satellite-derived [Chl-*a*] calculated with $R_{rs}(\lambda)$ band-ratio algorithms using the development dataset. In oceanic and moderately turbid coastal waters it is typical to use the ratio between a blue and a green band. Although this type of algorithms were shown to outperform semi-analytical ones in deriving [Chl-*a*] in oceanic and coastal waters (Brewin et al., 2015), they are known to be inadequate for coastal waters like the Chesapeake Bay (e.g., Magnuson et al., 2004; Tzortziou et al., 2007; Werdell et al., 2009). There are many variants of [Chl-*a*] algorithms that use blue-to-green band-ratio but the results from Brewin et al. (2015) show that their performances are fairly close. For simplicity, here we demonstrate the results of only the "OC2S" algorithm developed by O'Reilly et al. (2000),

$$[\text{Chl-}a] = 10^{0.2511-2.0853\,X+1.5035\,X^2-3.1747\,X^3+0.3383\,X^4}, \quad (1)$$

where $X = \log_{10}(R_{rs}(490)/R_{rs}(550))$. Figure 4 shows the OC2S-derived versus field-measured [Chl-*a*]. The correlation coefficient, *R*, which represents the overall goodness of agreement between the model-derived and measured data (original non-transformed, unless noted otherwise) over their dynamic range, is between 0.34 and 0.59 (more statistical parameters to be presented below). Le et al. (2013) found that red-to-green band ratios are better proxy of [Chl-*a*] over blue-to-green band ratios for the Chesapeake Bay waters. An advantage

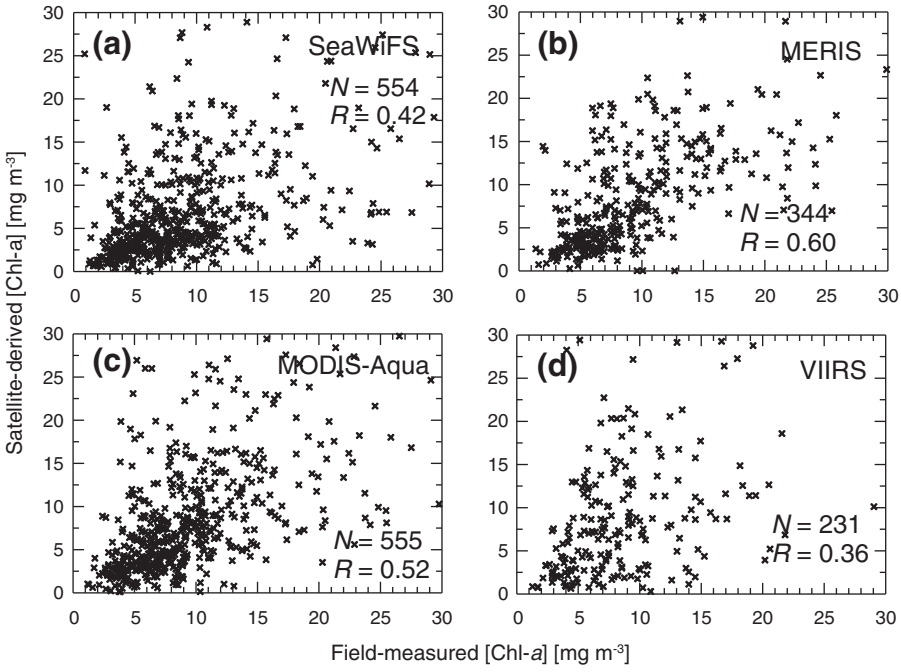

Fig. 5. Same as Fig. 4 except for using the red-to-green reflectance band ratios (a and b) $R_{rs}(670)/R_{rs}(510)$ (Eq. 2), (c) $R_{rs}(670)/R_{rs}(530)$ (Eq. 3), and (d) $R_{rs}(670)/R_{rs}(550)$ (Eq. 4), to obtain satellite-derived [Chl-*a*].

of using the red band around 670 nm is to minimize the interference caused by the light absorption of minerals and humus because at long wavelengths their absorption coefficients are spectrally minimal whereas phytoplankton still absorbs significantly. So we also compared the results of their formulas using the same matchup datasets, which include

$$[\text{Chl-}a] = 10^{2.96\,X+1.59}, \tag{2}$$

where $X = \log_{10}(R_{rs}(670)/R_{rs}(510))$

$$[\text{Chl-}a] = 10^{3.25\,X+2.09}, \tag{3}$$

where $X = \log_{10}(R_{rs}(670)/R_{rs}(530))$, and

$$[\text{Chl-}a] = 10^{4.38\,X+2.83}, \tag{4}$$

where $X = \log_{10}(R_{rs}(670)/R_{rs}(550))$. Here three different band ratios were chosen with each addressing a different sensor based on bands available to achieve the best possible performance as suggested by the results of Le et al. (2013). Figure 5 shows the results of these formulas. Compared with the blue-to-green band ratio algorithm, the *R* value is slightly improved for SeaWiFS, MODIS, and MERIS matchup data. The small improvement is in contrast with the significant improvement shown by Le et al. (2013) using field-measured $R_{rs}(\lambda)$ and [Chl-*a*] data as well as SeaWiFS and MODIS matchup data, possibly owing to the difference in testing datasets. For VIIRS data the *R* value actually degrades, suggesting that the performance of red-to-green band ratio algorithms might be sensor specific.

Another commonly used approach for deriving [Chl-*a*] in coastal waters is to contrast the $R_{rs}(\lambda)$ magnitudes between a NIR band and the red band. Here we used the two-band algorithm developed by Gitelson et al. (2007) with hyperspectral $R_{rs}(\lambda)$ data measured in the Chesapeake Bay as an example, which is.

$$[\text{Chl-}a] = 147.0R_{rs}(750)/R_{rs}(670) - 10.91. \tag{5}$$

We applied this algorithm to MODIS-Aqua (Fig. 6a) and VIIRS SWIR-corrected data (Fig. 6b), and found that the degree of correlation between the satellite-derived and field-measured [Chl-*a*] does not improve compared with using the visible band ratios. This is in contrast with previous studies that have demonstrated promising results using similar bands (e.g., Dall'Olmo et al., 2005; Gitelson et al., 2007; Gons et al., 2002; Moses et al., 2009). A key difference between our dataset and those used in previous studies is the dynamic range of [Chl-*a*]. Our matchup data are limited to [Chl-*a*] $< 30\ \text{mg m}^{-3}$, which is the most common range in the Chesapeake Bay surface waters (see Fig. 2), whereas the regression statistics between [Chl-*a*] and reflectance band ratios in other studies are largely driven by endmembers with much higher [Chl-*a*] ($> 100\ \text{mg m}^{-3}$). For these cases, the signal-to-noise ratio of the NIR-to-red reflectance band ratio is expected to be enhanced by stronger light absorption of phytoplankton compared to waters with lower algal biomass.

3.2. Revisiting the semi-analytical pathway to derive [Chl-a] from $a_{ph}(\lambda)$

The correlation coefficients between field-measured and satellite-derived [Chl-*a*] using reflectance band-ratio algorithms are low compared with regressions made with field-measured $R_{rs}(\lambda)$ data (e.g., Le et al., 2013; Tzortziou et al., 2007). This suggests that to some extent errors in satellite-measured $R_{rs}(\lambda)$ data likely affected the performance of these algorithms as shown in Figures 4–6. Additionally, another potential contributor of errors presumably arose from the interference by optically active nonalgal materials that vary independently with phytoplankton, such as terrestrial minerals and humus. Next, we evaluate the effectiveness of two algorithms that attempt to tease out this interference using the development dataset, namely the GSCM as well as the absorption-partitioning component of the QAA, both with the input of QAA-derived $a_{nw}(\lambda)$ data.

Figure 7 shows the GSCM-derived $a_{ph}(440)$ plotted versus field-measured [Chl-*a*]. We run a linear regression between the log-transformed data and the resultant correlation coefficient *R* ranges between 0.49 and 0.58, which is superior compared with the reflectance-band-ratio algorithms (Equations 1–4), as well as the QAA-derived $a_{ph}(440)$ (Fig. 7). The regression was made on log-transformed data because the relationship between $\log_{10}(a_{ph}(440))$ and $\log_{10}([\text{Chl-}a])$ were shown to be approximately linear over a broad range of [Chl-*a*] (Bricaud et al., 1995; Bricaud et al., 2004). The *R* values calculated for original non-transformed $a_{ph}(440)$ and [Chl-*a*] data are similar (0.44–0.57). However, for a large fraction of matchup data (~52–74%) the GSCM was unable to identify feasible solutions. We believe the most likely reason responsible for the null-solution scenario is associated with unrealistic spectral shape of the input $a_{nw}(\lambda)$, noticing that the satellite-derived $R_{rs}(\lambda)$ tends to be underestimated even after the quality screening

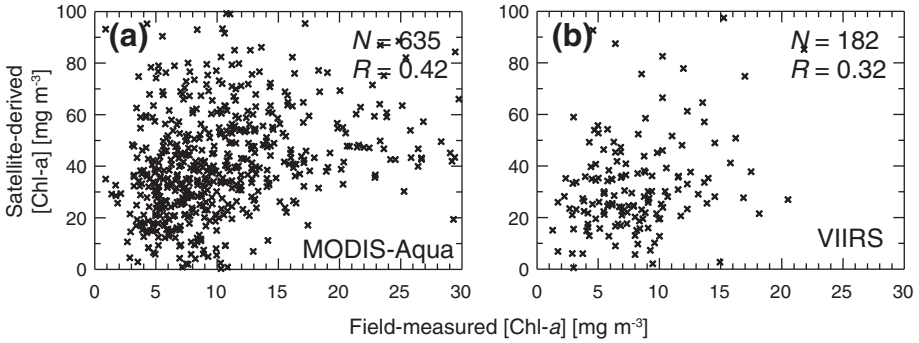

Fig. 6. Same as Fig. 4 except for using the NIR-to-red reflectance band ratio $R_{rs}(750)/R_{rs}(670)$ to obtain satellite-derived [Chl-*a*] (Eq. 5) and for (a) MODIS-Aqua and (b) VIIRS data obtained using the SWIR-bands as a basis for atmospheric correction.

process (Step 1 in Fig. 3) which leads to sudden jumps in the magnitude of QAA-derived $a_{nw}(\lambda)$ at the 410-nm band relative to the neighboring 440-nm band. Another potential reason may be because the built-in spectral shapes of $a_d(\lambda)$ and $a_g(\lambda)$ and the allowed ranges of variation of $a_{ph}(\lambda)$ within the GSCM are not sufficiently exhaustive and not always able to address the actual shapes of these absorption coefficients. However, this is less likely the case because the GSCM was always able to find feasible solutions when given the input of field-measured, i.e. generally better quality, $a_{nw}(\lambda)$ data (see Zheng et al., 2015).

Because the improvement in the *R*-value of GSCM-derived $a_{ph}(440)$ comes at the cost of significantly reduced data availability, one may wonder how much improvement can be achieved if the same set of inequality constraints as used in the GSCM are applied to QAA's outputs to reject infeasible solutions? We tested this hypothetical model and found that the resultant number of solutions was substantially (by ~90%, not shown) reduced, leading to much less number of outputs even compared with the GSCM. What happened was that owing to the fixed spectral shape (exponential function of λ) used by QAA to parameterize the sum of $a_d(\lambda) + a_g(\lambda)$, other non-exponential but potentially more realistic spectral shapes (such as those used in the GSCM) do not even have a chance to be considered in the search for feasible solutions from QAA's outputs. Thus, the capability to reject problematic solutions is actually a unique feature of the GSCM.

Compared with the blue band, the GSCM-derived $a_{ph}(\lambda)$ at the red band (~670 nm) is correlated better with field-measured [Chl-*a*] (Fig. 8), with correlation coefficient *R* between log-transformed data ranging within 0.54–0.66. The QAA-derived $a_{ph}(670)$ is also much improved compared with the results at 440 nm, and outperforms the OC2S algorithm in terms of the degree of correlation with field-measured [Chl-*a*]. The stronger correlation at the red band is associated with the lower variability of the pigment-packaging effect at the red band than at the blue band. In addition, accessory pigments (contribute to $a_{ph}(\lambda)$ but not to [Chl-*a*]) absorb mainly in the blue and generally negligibly in the red, which helps further constrain the relationship between $a_{ph}(670)$ and [Chl-*a*]. Therefore, the red band appears to be a better option than the blue band to derive [Chl-*a*] from the GSCM-derived $a_{ph}(\lambda)$ for waters in the Chesapeake Bay. Note that in the round-robin test conducted by Brewin et al. (2015) the $a_{ph}(440)$ was used to derive [Chl-*a*] owing to the low signal of phytoplankton absorption at ~670 nm in typical oceanic waters compared with pure water absorption.

Based on the analyses above, we revisit the pathway adopted by semi-analytical models for deriving the [Chl-*a*] from $R_{rs}(\lambda)$ via the derivation of $a_{ph}(\lambda)$, and propose to use the GSCM as the method for obtaining $a_{ph}(\lambda)$ from QAA-derived $a_{nw}(\lambda)$. Our results suggest that introducing the GSCM to this pathway effectively improved the correlation between satellite-derived $a_{ph}(\lambda)$ and field-measured [Chl-*a*], despite of restrictive assumptions made by the QAA to derive $a_{nw}(\lambda)$ from $R_{rs}(\lambda)$ as well as relatively large uncertainties in satellite-measured $R_{rs}(\lambda)$ data in coastal waters such as the Chesapeake Bay. In addition, the use of the red band appears to be advantageous over the blue band for moderate levels of [Chl-*a*] common to this estuary. If data quality

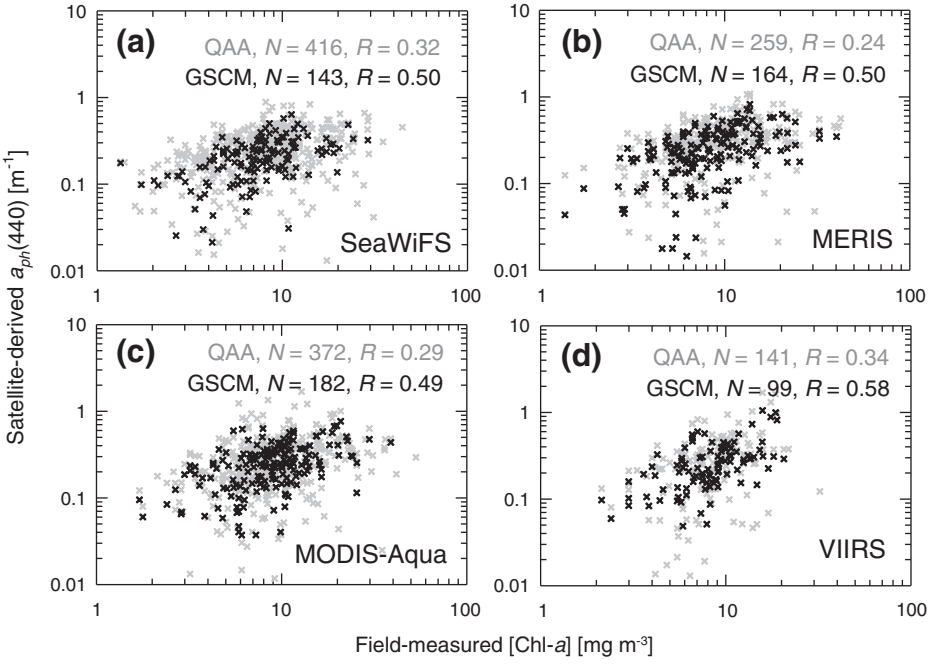

Fig. 7. Phytoplankton absorption coefficient, $a_{ph}(440)$, derived from (a) SeaWiFS, (b) MERIS, (c) MODIS-Aqua, and (d) VIIRS data, plotted versus field-measured chlorophyll concentration in the Chesapeake Bay. The black and gray crosses denote the $a_{ph}(440)$ obtained with the GSCM (see Steps 1 through 3 in Fig. 3) and with only the QAA (see Steps 1 and 2 in Fig. 3), respectively. *R*, correlation coefficient between log-transformed data. Note that for the QAA-derived results a significant portion (~25–40%) of negative $a_{ph}(440)$ values were excluded from the regression after the log transformation.

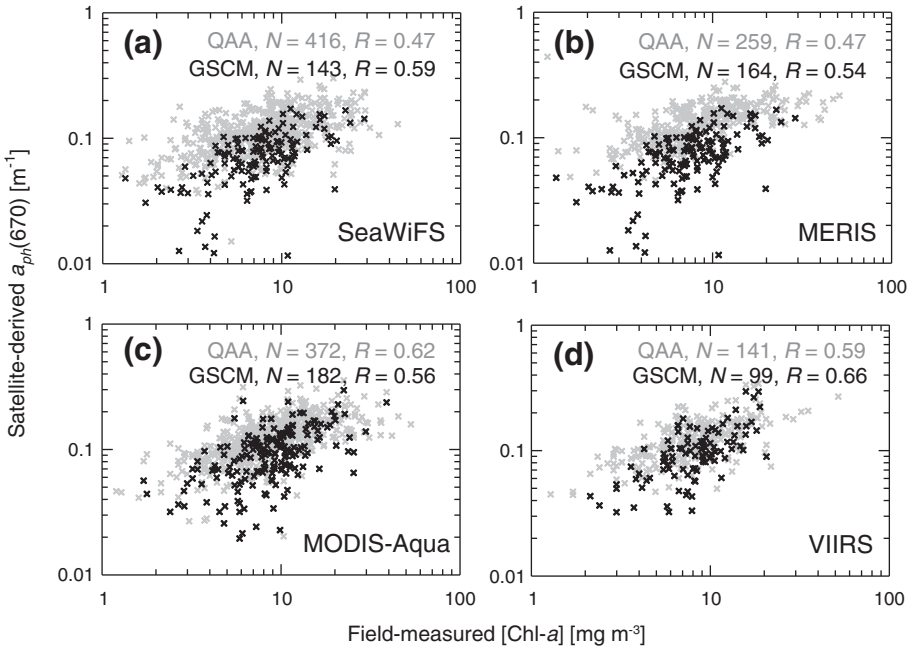

Fig. 8. Same as Fig. 7 except for the phytoplankton absorption coefficient $a_{ph}(670)$.

rather than quantity is the priority, at the present stage we recommend the following specific pathway for remote sensing of [Chl-*a*] in the Chesapeake Bay and other coastal waters alike,

$$R_{rs}(\lambda) \rightarrow \text{QAA-derived } a_{nw}(\lambda) \rightarrow \text{GSCM-derived } a_{ph}(670) \rightarrow [\text{Chl-}a].$$

A key formula in this pathway is the conversion of $a_{ph}(670)$ to [Chl-*a*]. Here we make an assumption that an average $a_{ph}^*(670)$ can be applied to most surface waters in the Chesapeake Bay. While this assumption clearly has room for improvements to account for variations in pigment-packaging effect, based on current quality of satellite data we could not identify other independent information that may indicate changes in $a_{ph}^*(670)$. For instance, the spectral shape of GSCM-derived $a_{ph}(\lambda)$ such as the ratio of $a_{ph}(670)$:$a_{ph}(440)$ may be used to tell the pigment-packaging effect to a certain degree, but we checked and found no meaningful relationship between this ratio and $a_{ph}^*(670)$. Nonetheless, we consider pigment-packaging effect a secondary factor at 670 nm for derivation of [Chl-*a*], and the main focus of this study is not to solve all problems in remote sensing of [Chl-*a*], but to address the question of whether satellite [Chl-*a*] product can be improved simply by improving the derived $a_{ph}(670)$, which should be the case in theory since reflectance-band-ratio algorithms do not address the pigment-packaging effect either.

So we conducted a linear regression between the two variables combining the matchup data from all four sensors in the development dataset (Fig. 9a). Several outliers were excluded in this regression analysis, which were identified by dividing all data points into three arbitrary groups based on the ratio of $a_{ph}(670)$:$a_{ph}(440)$, and then picking out the ones that deviate by > 50% from the linear regression curve of each group. We also forced the intercept to zero based on the assumption that there should be no phytoplankton light absorption at 670 nm when [Chl-*a*] is zero. The final relationship is,

$$[\text{Chl-}a] = a_{ph}(670)/0.010 \quad (6)$$

The coefficient of 0.010 $m^2\,mg^{-1}$ has a significant physical meaning which is the average chlorophyll-specific phytoplankton absorption coefficient at the 670 nm, $a_{ph}^*(670)$, in the Chesapeake Bay surface waters. The $a_{ph}^*(670)$ derived from satellite data using our approach is only about half of the field-measured values reported by Magnuson et al. (2004, see their Fig. 4), and on the lower end of a global dataset reported by Bricaud et al. (1995) where $a_{ph}^*(675)$ varies roughly within 0.01–0.03 $m^2\,mg^{-1}$ for [Chl-*a*] > 1 mg m^{-3}, as well as values in European coastal waters reported by Babin et al. (2003). Compared with a "theoretical" upper limit of $a_{ph}^*(675)$ = 0.0207 mg m^{-3} for pure dissolved Chl-*a* (Bricaud et al., 1983), which can only be approached by the smallest pico-phytoplankton found in oligotrophic waters, the $a_{ph}^*(670)$ values reported by Magnuson et al. (2004) may appear too high for phytoplankton in eutrophic waters like the Chesapeake Bay which is generally dominated by diatoms known to have stronger pigment-packaging effect (Magnuson et al., 2004; Sathyendranath et al., 2004; Stuart et al., 2000). However, field-measured $a_{ph}^*(670)$ for natural phytoplankton assemblages can be contributed by the light absorption of total chlorophyll-*b* (Bricaud et al., 1995) and exceedance of 0.0207 mg m^{-3} is likely reasonable, although field-measured $a_{ph}(\lambda)$ and [Chl-*a*] data are both subject to their own uncertainties. With respect to satellite-derived $a_{ph}(670)$, we note that our approach by partitioning the QAA-derived $a_{nw}(670)$ might have underestimated it because the QAA-derived $a_{nw}(670)$ is systematically underestimated (based on field-measured data in the Chesapeake Bay, not shown here). This suggests that the use of 670 nm as a reference band in the QAA may not be always adequate for more turbid endmembers in the Chesapeake Bay, consistent with the studies by Le et al. (2009) and Yang et al. (2013) that moving the reference band to the NIR improves the performance of QAA in turbid lake waters. In summary, the value of 0.010 $m^2\,mg^{-1}$ in Eq. (6) may not be the most robust estimation of $a_{ph}^*(670)$ for Chesapeake Bay surface waters but more of a practical choice that compensates for bias in satellite-derived $a_{ph}(670)$ obtained with the data and methods we used.

Although QAA itself does not provide a [Chl-*a*] formula, the Eq. (6) obtained for GSCM-derived $a_{ph}(670)$ can be used for QAA-derived $a_{ph}(670)$ as well. A regression analysis between QAA-derived $a_{ph}(670)$ and field-measured [Chl-*a*] yielded the same coefficient as Eq. (6) by coincidence (not shown).

3.3. Evaluation of $a_{ph}(\lambda)$- and $R_{rs}(\lambda)$-based [Chl-*a*] algorithms for Chesapeake Bay waters

To evaluate the accuracy of the [Chl-*a*] product derived with the recommended pathway involving Eq. (6), we first examined a comprehensive set of statistical error parameters calculated using the

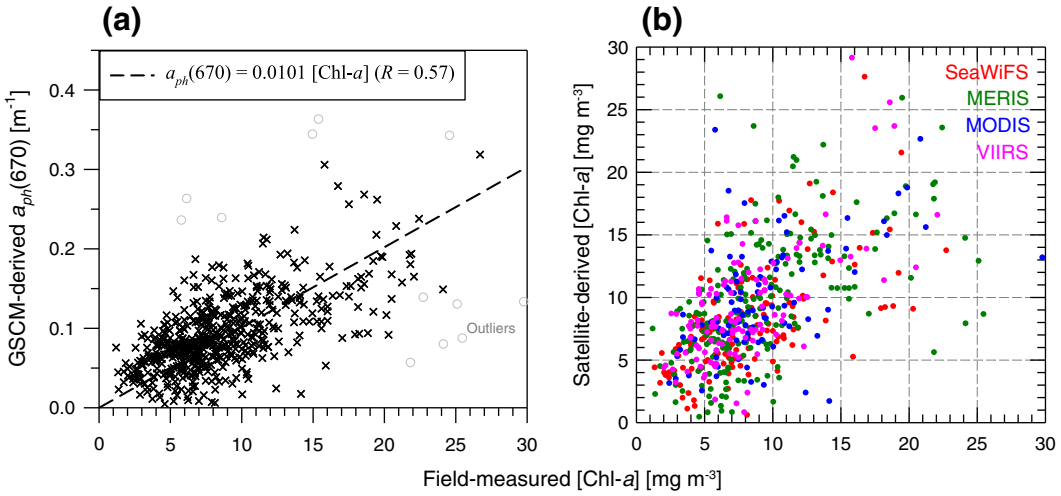

Fig. 9. (a) Linear regression between field-measured [Chl-a] and satellite-derived $a_{ph}(670)$ obtained by partitioning the QAA-derived $a_{nw}(\lambda)$ using the GSCM using the development dataset. (b) [Chl-a] derived using the regression formula shown in (a) plotted against the field-measured values. (For interpretation of the references to color in this figure legend, the reader is referred to the web version of this article.)

Table 1
Summary of error statistics for model-derived [Chl-a] for the development dataset (1997–2015). N is the number of observations used for calculating the error statistics. R is the correlation coefficient calculated for original non-transformed data. The *MR* is the median ratio of model-derived to measured values, and SIQR is the semi-interquartile range for this ratio calculated as $SIQR = (QR_3 - QR_1) / 2$, where QR_1 is the first quartile and QR_3 is the third quartile of this ratio. Slope is the linear slope obtained from Model II regression (Pearson's Major Axis) between model-derived and measured values. The *MPD* is the median absolute percent difference calculated as the median of the individual absolute percent differences, $PD_i = 100\,|Y_i - X_i| / X_i$, where Y_i is the model-derived and X_i is the measured value. The *RMSD* is the root mean square deviation between these data.

Model	Equation	Sensor	*N*	*R*	*MR*	*SIQR*	Slope	*MPD* (%)	*RMSD* (mg m^{-3})
OC2S	(1)	SeaWiFS	554	0.40	1.03	0.42	1.50	39	7.0
		MERIS	345	0.48	1.09	0.44	0.76	40	7.1
		MODIS-Aqua	555	0.34	1.02	0.42	0.63	38	7.0
		VIIRS	231	0.59	1.12	0.34	0.93	33	5.3
By Le et al. (2013)	(2)	SeaWiFS	554	0.42	0.66	0.32	1.22	48	6.8
		MERIS	344	0.60	0.77	0.29	0.86	39	6.5
	(3)	MODIS-Aqua	555	0.52	0.80	0.32	1.48	40	7.3
	(4)	VIIRS	231	0.36	0.96	0.58	7.65	54	17.5
By Gitelson et al. (2007)	(5)	MODIS-Aqua	634	0.42	3.80	1.82	7.48	280	43.8
		VIIRS	181	0.32	3.31	1.89	12.05	290	35.2
Using QAA-derived $a_{ph}(670)$	(6)	SeaWiFS	416	0.44	1.43	0.45	0.45	48	5.9
		MERIS	259	0.52	1.42	0.41	0.47	48	6.6
		MODIS-Aqua	372	0.48	1.42	0.39	0.50	46	6.8
		VIIRS	141	0.54	1.46	0.40	1.44	48	6.0
Using GSCM-derived $a_{ph}(670)$	(6)	SeaWiFS	143	0.59	0.96	0.32	0.61	31	3.8
		MERIS	164	0.54	1.06	0.37	0.63	34	5.3
		MODIS-Aqua	182	0.56	1.08	0.32	0.82	32	4.8
		VIIRS	99	0.66	1.20	0.32	1.47	31	4.2

development dataset in comparison with other models discussed above, assuming that the differences between the satellite/model-derived and field-measured [Chl-a] can be considered to represent errors of the models. Note that development dataset is only dependent for the $a_{ph}(\lambda)$-based models (i.e., QAA- and GSCM-derived). The parameters of all $R_{rs}(\lambda)$-based [Chl-a] algorithms (Equations 1–5) were previously obtained with other datasets and therefore these algorithms are independent from the development dataset of this study. The following error parameters were calculated: The median of the ratio of model-derived to measured values, *MR*, was calculated to provide a measure of overall bias in the modeled data relative to measurements. The semi-interquartile range, *SIQR*, calculated for the ratio of modeled-derived to measured values indicates the spread of the modeled data from measurements. The slope of a Model II linear regression (major axis) between model-derived and measured values indicates the proportional systematic error of model-derived values. The overall degree of agreement between the model and measurements is provided by the median value of the absolute percent difference, *MPD*, between the model-derived and measured data and also by the root mean square deviation (*RMSD*) between these data.

Table 1 summarizes these error statistics for [Chl-a]. Compared with the blue-to-green reflectance-band-ratio algorithm (Eq. 1), the [Chl-a] derived from Eq. (6) using the GSCM-derived $a_{ph}(670)$ provides generally improved results, particularly for error statistics driven more by random errors. In addition to the improved R as discussed above, the *SIQR* decreased from 0.34–0.44 to 0.32–0.37, the *MPD* decreased from 33 to 40% to 31–34%, and the *RMSD* decreased from 5.3–7.1 mg m^{-3} to 3.8–5.3 mg m^{-3}. Error statistics represented by the *MR* and slope parameters exhibited no improvements, which is because they are driven mainly by systematic errors whereas the regression to obtain Eq. (6) was not the best possible fit to data in an effort to force the intercept to zero. When it comes to the comparison between the red-to-green reflectance-band-ratio algorithms (Equations 2–4) and Eq. (6) using the GSCM-derived $a_{ph}(670)$, the *SIQR* values characterizing the spread of data are quite close except for VIIRS data, and for other error statistics the GSCM-derived results are generally better. Note that the [Chl-a] obtained with QAA-derived $a_{ph}(670)$ are not improved compared with blue-to-green and red-to-green reflectance-band-ratio algorithms

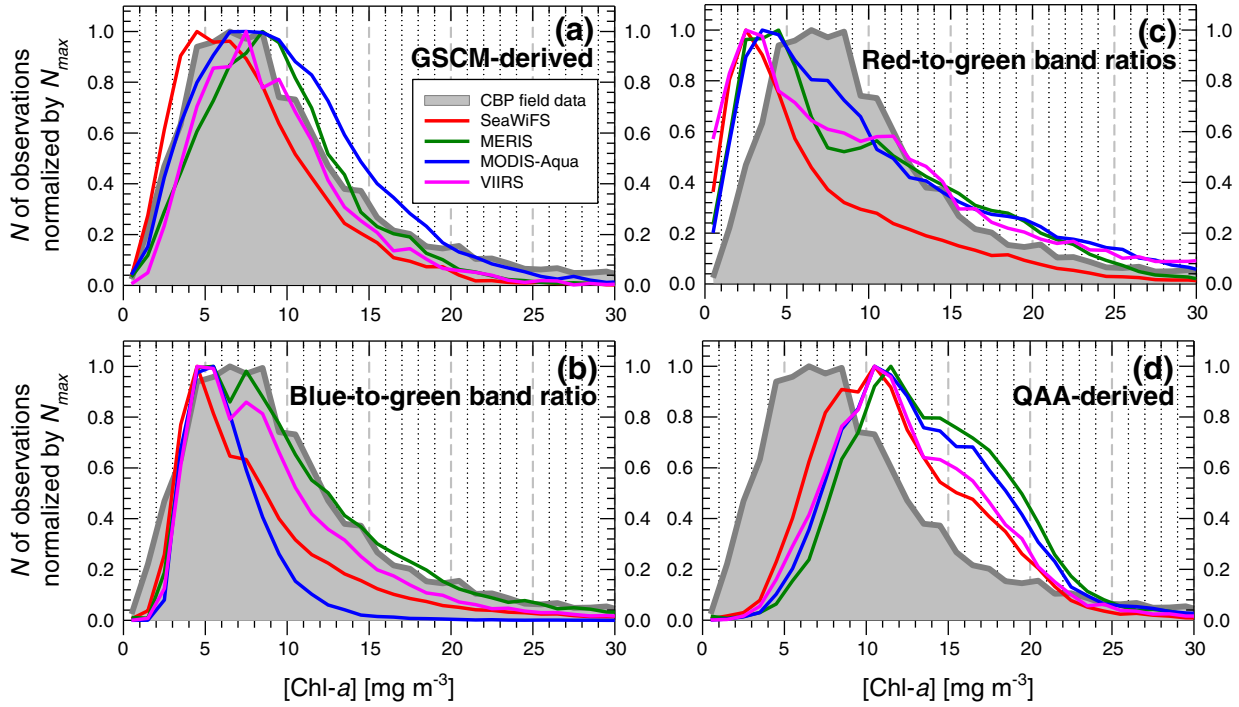

Fig. 10. Comparisons of normalized histograms between field-measured and satellite-derived [Chl-*a*] data obtained at field-sampling stations (see Fig. 1) during 1997–2015. Satellite histograms (color curves) are based on [Chl-*a*] calculated with (a) the GSCM-derived $a_{ph}(670)$ (Eq. 6), (b) the OC2S blue-to-green reflectance band-ratio algorithm (Eq. 1), (c) the red-to-green reflectance band-ratio algorithms (Eqs. 2–4), and (d) the QAA-derived $a_{ph}(670)$ (Eq. 6). The field data histogram (gray curve with shade) is redrawn from Fig. 2 except with higher bin resolution (every 1 mg m^{-3}). N_{max}, the maximum number of observations per bin among all bins. CBP, Chesapeake Bay Program. (For interpretation of the references to color in this figure legend, the reader is referred to the web version of this article.)

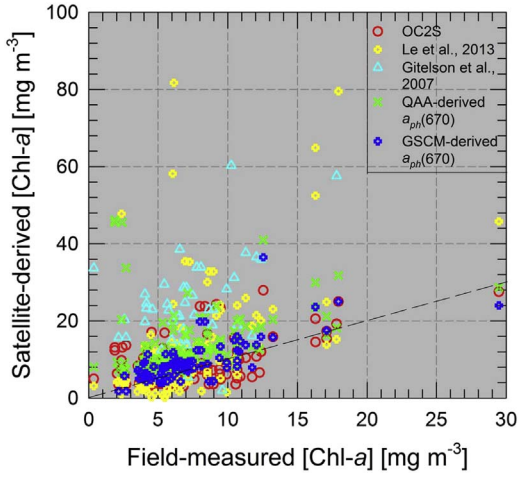

Fig. 11. Comparison of different [Chl-*a*] algorithms using the validation dataset consisting of 2016 data. Note that only VIIRS is included in satellite data, and that most VIIRS data were BMW-corrected, except for the model by Gitelson et al. (2007) which was based on SWIR-corrected. (For interpretation of the references to color in this figure legend, the reader is referred to the web version of this article.)

(Equations 1–4). The NIR-to-red reflectance-band-ratio algorithm (Eq. 5) exhibits significantly larger errors than all other models.

To provide additional circumstantial evidence for evaluating the performance of the recommended pathway, we also examined the histogram of all satellite-derived [Chl-*a*] at the same locations where CBP field data were collected. Figure 10a shows that for all four sensors the GSCM-derived [Chl-*a*] using Eq. (6) provides quite close histograms compared with field-measured [Chl-*a*] data, which is not the case for with other models (Fig. 10b – d). This suggest that the proposed pathway may also facilitate the construction of a merged [Chl-*a*] dataset using multiple sensors.

We further evaluated the performance of the proposed pathway with the validation dataset comprising VIIRS $R_{rs}(\lambda)$ data and CBP [Chl-*a*] data obtained in 2016 which is independent from Eq. (6). A total of 130 matchups were identified for VIIRS BMW-corrected data, and 57 for SWIR-corrected data. Significantly less number of matchups were obtained for SWIR-corrected data because more spectra were rejected in the quality-screening process (Step 1 in Fig. 3). Figure 11 and Table 2 show the result in comparison with other algorithms. Compared with the development dataset, the GSCM-derived results show consistent performance when evaluated against the validation dataset. Compared with the OC2S algorithm, the error statistics calculated for results of Eq. (6) using GSCM-derived $a_{ph}(670)$ are generally better or comparable except the *MR* parameter which characterizes the systematic error. This

Table 2
Same as Table 1 but for the validation dataset obtained by matching up CBP field-measured with VIIRS observations in 2016 (the same data shown in Fig. 11).

Model	Equation	*N*	*R*	*MR*	*SIQR*	Slope	*MPD* (%)	*RMSD* (mg m^{-3})
OC2S	(1)	130	0.57	1.03	0.38	1.44	32	5.0
By Le et al. (2013)	(4)	130	−0.18	1.37	0.77	−271.17	59	228.0
By Gitelson et al. (2007)	(5)	57	0.26	2.85	1.60	56.02	229	44.3
Using QAA-derived $a_{ph}(670)$	(6)	130	0.33	1.72	0.44	3.85	72	10.3
Using GSCM-derived $a_{ph}(670)$	(6)	92	0.72	1.31	0.23	1.25	33	4.5

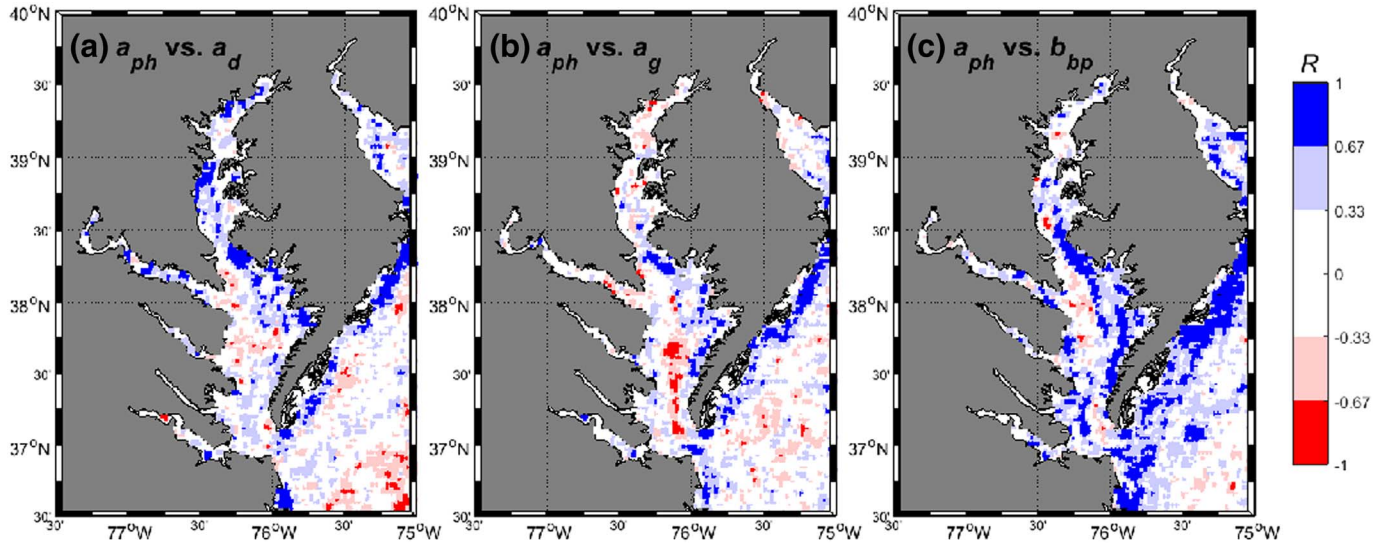

Fig. 12. Small scale spatial correlation coefficient between (a) $a_{ph}(440)$ and $a_d(440)$, (b) $a_{ph}(440)$ and $a_g(440)$, and (c) $a_{ph}(440)$ and $b_{bp}(440)$, calculated with VIIRS summer climatology (2012–2015). (For interpretation of the references to color in this figure legend, the reader is referred to the web version of this article.)

again is because the regression to obtain Eq. (6) was not the best possible fit to the development dataset, and the fit was made for four satellite sensors and not optimized for VIIRS. The most significant improvement was the *SIQR* parameter which is nearly half of that for OC2S retrievals, suggesting that the GSCM-derived [Chl-*a*] retrievals are much "tighter". The OC2S algorithm performs the best among all $R_{rs}(\lambda)$-based models, although the models by Le et al. (2013) and Gitelson et al. (2007) were parameterized specifically for the Chesapeake Bay whereas the OC2S model used a global parameterization. In particular, the systematic error represented by *MR* for the globally parameterized OC2S model is actually lower than other models which are all "customized" for the Chesapeake Bay. These evidences suggest that the main factor that affects the performance comparison here is not model parameterization, but more likely the functional form.

It is worth to note an important feature of the GSCM-derived [Chl-*a*]: It is essentially decoupled from non-phytoplankton absorption components. We compared the VIIRS summer seasonal mean climatologies (averaged for 2012–2015) of the GSCM-derived $a_{ph}(440)$, $a_d(440)$, $a_g(440)$, and the QAA-derived $b_{bp}(440)$, and calculated the spatial correlation coefficient among them at small scales (± 5 km). Figure 12 shows the $a_{ph}(440)$ (and hence the derived [Chl-*a*]) exhibits variable and generally low correlation with $a_d(440)$, $a_g(440)$, and $b_{bp}(440)$ in summer in the Chesapeake Bay. This feature allows the study of potentially independent variations of different biogeochemical/water quality parameters, which would not be possible when these parameters are derived from the same reflectance band ratios.

4. Conclusions

Although at the cost of heavily lost data availability, deriving [Chl-*a*] based on GSCM-derived $a_{ph}(670)$ can provide higher-quality results over empirical reflectance-band-ratio algorithms for the Chesapeake Bay waters. This is encouraging considering potential errors associated with satellite-measured $R_{rs}(\lambda)$ data (particularly those that distort its spectral shape) and restrictive assumptions made by the upstream model, QAA, which provided input $a_{nw}(\lambda)$ data for the GSCM. The success also highlights the significance of improving the attribution of total light absorption coefficient to phytoplankton and nonalgal components for bio-optical remote sensing in coastal waters. For typical water conditions in the Chesapeake Bay and likely most coastal waters, a robust absorption-partitioning algorithm is helpful for retrieving phytoplankton information if data quality as opposed to quantity is considered a priority. This type of algorithms is also critical for conducting other advanced water quality applications such as assessment of CDOM and suspended sediment loadings.

Application of the GSCM to satellite ocean color data reveals one pertinent issue of null feasible solutions which makes it unsuitable for operational use at the present stage and needs to be resolved in future research. The GSCM works on the principle of interpreting the spectral shape of $a_{nw}(\lambda)$ in a wide variety of ways. In the remote-sensing context, whether feasible solutions can be found ultimately boils down to the spectral shape of $R_{rs}(\lambda)$, the upstream model that derives the $a_{nw}(\lambda)$, and the generality of the GSCM itself. To enable GSCM to identify feasible solutions for more satellite pixels, the key is to ensure that the actual spectral shape of input $a_{nw}(\lambda)$ is well preserved in the entire visible spectrum. This we believe should be an important research direction for the future. Specifically, we suggest addressing the following three topics: 1) Improve the atmospheric correction to obtain high-quality $R_{rs}(\lambda)$ data in coastal waters, particularly for the blue bands. 2) Develop a new model to derive $a_{nw}(\lambda)$ from $R_{rs}(\lambda)$ which does not involve any restrictive assumptions, consistent with the stacked-constraints concept from end to end. 3) Improve the generality of the GSCM in the Chesapeake Bay mainly by adding more types of representative spectra of $a_d(\lambda)$ and $a_g(\lambda)$ to its library as needed. With respect to the applicability of the current version of GSCM to other coastal waters, it depends on the similarity in bio-geo-optical properties compared with the Chesapeake Bay. The GSCM can always be applied to other regions but the application is best made when backed by local field data to ensure that the representative spectra of $a_d(\lambda)$ and $a_g(\lambda)$ and the defined ranges of $a_{ph}(\lambda)$ band ratios are truly representative to the region of interest.

Acknowledgements

This work was supported by NOAA's Ocean Remote Sensing (ORS) Program. We thank NASA/GSFC/OBPG for providing SeaWiFS, MERIS, and MODIS data. We are in debt to Lide Jiang, Karlis Mikelsons, and Menghua Wang in NOAA/STAR/SOCD for providing VIIRS BMW- and SWIR-corrected data, and SeungHyun Son for providing MODIS-Aqua SWIR-corrected data. We are grateful to all scientists, crew, and staff who collected the field data and made them available through the Chesapeake Bay Program databases. The contents of this article are solely the opinions of the authors and do not constitute a statement of policy, decision, or position on behalf of the NOAA or the U.S. Government.

References

Aas, E., 1996. Refractive index of phytoplankton derived from its metabolite composition. J. Plankton Res. 18, 2223–2249.

Alimonte, D.D., Zibordi, G., 2003. Phytoplankton determination in an optically complex coastal region using a multilayer perceptron neural network. IEEE Trans. Geosci. Remote Sens. 41, 2861–2868.

ASTM, 2012. Standard Practices for Measurement of Chlorophyll Content of Algae in Surface Waters. In. West Conshohocken, Pennsylvania.

Babin, M., Stramski, D., Ferrari, G.M., Claustre, H., Bricaud, A., Obolensky, G., Hoepffner, N., 2003. Variations in the light absorption coefficients of phytoplankton, nonalgal particles, and dissolved organic matter in coastal waters around Europe. J. Geophys. Res. 108, 3211.

Bailey, S.W., Franz, B.A., Werdell, P.J., 2010. Estimation of near-infrared water-leaving reflectance for satellite ocean color data processing. Opt. Express 18, 7521–7527.

Brewin, R.J.W., Sathyendranath, S., Müller, D., Brockmann, C., Deschamps, P.-Y., Devred, E., Doerffer, R., Fomferra, N., Franz, B., Grant, M., Groom, S., Horseman, A., Hu, C., Krasemann, H., Lee, Z., Maritorena, S., Mélin, F., Peters, M., Platt, T., Regner, P., Smyth, T., Steinmetz, F., Swinton, J., Werdell, J., White Iii, G.N., 2015. The ocean colour climate change initiative: III. A round-robin comparison on in-water bio-optical algorithms. Remote Sens. Environ. 162, 271–294.

Bricaud, A., Morel, A., Prieur, L., 1983. Optical efficiency factors of some phytoplankters. Limnol. Oceanogr. 28, 816–832.

Bricaud, A., Babin, M., Morel, A., Claustre, H., 1995. Variability in the chlorophyll-specific absorption coefficients of natural phytoplankton: analysis and parameterization. J. Geophys. Res. 100, 13321–13332.

Bricaud, A., Claustre, H., Ras, J., Oubelkheir, K., 2004. Natural variability of phytoplanktonic absorption in oceanic waters: influence of the size structure of algal populations. J. Geophys. Res. 109 C11010.

Dall'Olmo, G., Gitelson, A.A., Rundquist, D.C., Leavitt, B., Barrow, T., Holz, J.C., 2005. Assessing the potential of SeaWiFS and MODIS for estimating chlorophyll concentration in turbid productive waters using red and near-infrared bands. Remote Sens. Environ. 96, 176–187.

Dickey, T., Lewis, M., Chang, G., 2006. Optical oceanography: recent advances and future directions using global remote sensing and in situ observations. Rev. Geophys. 44 RG1001.

Gitelson, A.A., Schalles, J.F., Hladik, C.M., 2007. Remote chlorophyll-a retrieval in turbid, productive estuaries: Chesapeake Bay case study. Remote Sens. Environ. 109, 464–472.

Gons, H.J., Rijkeboer, M., Ruddick, K.G., 2002. A chlorophyll-retrieval algorithm for satellite imagery (Medium Resolution Imaging Spectrometer) of inland and coastal waters. J. Plankton Res. 24, 947–951.

González Vilas, L., Spyrakos, E., Torres Palenzuela, J.M., 2011. Neural network estimation of chlorophyll a from MERIS full resolution data for the coastal waters of Galician rias (NW Spain). Remote Sens. Environ. 115, 524–535.

Jiang, L., Wang, M., 2014. Improved near-infrared ocean reflectance correction algorithm for satellite ocean color data processing. Opt. Express 22, 21657–21678.

Le, C.F., Li, Y.M., Zha, Y., Sun, D., Yin, B., 2009. Validation of a quasi-analytical algorithm for highly turbid eutrophic water of Meiliang Bay in Taihu Lake, China. IEEE Trans. Geosci. Remote Sens. 47, 2492–2500.

Le, C., Hu, C., Cannizzaro, J., Duan, H., 2013. Long-term distribution patterns of remotely sensed water quality parameters in Chesapeake Bay. Estuar. Coast. Shelf Sci. 128, 93–103.

Lee, Z., Carder, K.L., Arnone, R.A., 2002. Deriving inherent optical properties from water color: a multiband quasi-analytical algorithm for optically deep waters. Appl. Opt. 41, 5755–5772.

Magnuson, A., Harding Jr., L.W., Mallonee, M.E., Adolf, J.E., 2004. Bio-optical model for Chesapeake Bay and the middle Atlantic bight. Estuar. Coast. Shelf Sci. 61, 403–424.

Maritorena, S., Siegel, D.A., Peterson, A.R., 2002. Optimization of a semianalytical ocean color model for global-scale applications. Appl. Opt. 41, 2705–2714.

Mitchell, C., Cunningham, A., McKee, D., 2014. Remote sensing of shelf sea optical properties: evaluation of a quasi-analytical approach for the Irish Sea. Remote Sens. Environ. 143, 142–153.

Moses, W.J., Gitelson, A.A., Berdnikov, S., Povazhnyy, V., 2009. Satellite estimation of chlorophyll-a concentration using the red and NIR bands of MERIS & #x2014; The Azov Sea case study. IEEE Geosci. Remote Sens. Lett. 6, 845–849.

Olson, M., 2012. Guide to Using Chesapeake Bay Program Water Quality Monitoring Data. In M. Mallonee, & Me.E. Ley (Eds.) Annapolis, Maryland.

O'Reilly, J.E., Maritorena, S., Mitchell, B.G., Siegel, D.A., Carder, K.L., Garver, S.A., Kahru, M., McClain, C., 1998. Ocean color chlorophyll algorithms for SeaWiFS. J. Geophys. Res. 103, 24937–24953.

O'Reilly, J.E., Maritorena, S., Siegel, D.A., O'Brien, M.C., Toole, D., Mitchell, B.G., Kahru, M., Chavez, F.P., Strutton, P., Cota, G.F., Hooker, S.B., 2000. Ocean color chlorophyll a algorithms for SeaWiFS, OC2, and OC4: version 4. In: Toole, D., Mitchell, B.G., Kahru, M., Chavez, F.P., Strutton, P., Cota, G., Hooker, S.B., McClain, C.R., Carder, K.L., Muller-Karger, F., Harding, L., Magnuson, A., Phinney, D., Moore, G.F., Aiken, J., Arrigo, K.R., Letelier, R., Culver, M., Hooker, S.B., Firestone, E.R. (Eds.), SeaWiFS Postlaunch Calibration and Validation Analyses, Part, 3. NASA, Goddard Space Flight Center, Greenbelt, Maryland, pp. 9–23.

Ruddick, K.G., Ovidio, F., Rijkeboer, M., 2000. Atmospheric correction of SeaWiFS imagery for turbid coastal and inland waters. Appl. Opt. 39, 897–912.

Sathyendranath, S., Watts, L., Devred, E., Platt, T., Caverhill, C., Maass, H., 2004. Discrimination of diatoms from other phytoplankton using ocean-colour data. Mar. Ecol. Prog. Ser. 272, 59–68.

Smyth, T.J., Moore, G.F., Hirata, T., Aiken, J., 2006. Semianalytical model for the derivation of ocean color inherent optical properties: description, implementation, and performance assessment. Appl. Opt. 45, 8116–8131.

Stramski, D., Kiefer, D.A., 1991. Light scattering by microorganisms in the open ocean. Prog. Oceanogr. 28, 343–383.

Stramski, D., Boss, E., Bogucki, D., Voss, K.J., 2004. The role of seawater constituents in light backscattering in the ocean. Prog. Oceanogr. 61, 27–56.

Stuart, V., Sathyendranath, S., Head, E.J.H., Platt, T., Irwin, B., Maass, H., 2000. Bio-optical characteristics of diatom and prymnesiophyte populations in the Labrador Sea. Mar. Ecol. Prog. Ser. 201, 91–106.

Tanaka, A., Kishino, M., Doerffer, R., Schiller, H., Oishi, T., Kubota, T., 2004. Development of a neural network algorithm for retrieving concentrations of chlorophyll, suspended matter and yellow substance from radiance data of the ocean color and temperature scanner. J. Oceanogr. 60, 519–530.

Tzortziou, M., Subramaniam, A., Herman, J.R., Gallegos, C.L., Neale, P.J., Harding, L.W., 2007. Remote sensing reflectance and inherent optical properties in the mid Chesapeake Bay. Estuar. Coast. Shelf Sci. 72, 16–32.

Wang, M.H., Tang, J.W., Shi, W., 2007. MODIS-derived ocean color products along the China east coastal region. Geophys. Res. Lett. 34, L06611.

Wang, M., Shi, W., Jiang, L., 2012. Atmospheric correction using near-infrared bands for satellite ocean color data processing in the turbid western Pacific region. Opt. Express 20, 741–753.

Wei, J., Lee, Z., Shang, S., 2016. A system to measure the data quality of spectral remote-sensing reflectance of aquatic environments. J. Geophys. Res. 121, 8189–8207.

Werdell, P.J., Bailey, S.W., Franz, B.A., Harding Jr., L.W., Feldman, G.C., McClain, C.R., 2009. Regional and seasonal variability of chlorophyll-a in Chesapeake Bay as observed by SeaWiFS and MODIS-aqua. Remote Sens. Environ. 113, 1319–1330.

Yang, W., Matsushita, B., Chen, J., Yoshimura, K., Fukushima, T., 2013. Retrieval of inherent optical properties for turbid inland waters from remote-sensing reflectance. IEEE Trans. Geosci. Remote Sens. 51, 3761–3773.

Zheng, G., Stramski, D., Reynolds, R.A., 2014. Evaluation of the quasi-analytical algorithm for estimating the inherent optical properties of seawater from ocean color: comparison of Arctic and lower-latitude waters. Remote Sens. Environ. 155, 194–209.

Zheng, G.M., Stramski, D., DiGiacomo, P.M., 2015. A model for partitioning the light absorption coefficient of natural waters into phytoplankton, nonalgal particulate, and colored dissolved organic components: a case study for the Chesapeake Bay. J. Geophys. Res. 120, 2601–2621.